

Molecular dynamics simulations of the delta and omicron SARS-CoV-2 spike – ACE2 complexes reveal distinct changes between both variants

Eileen Socher

Friedrich-Alexander-University Erlangen-Nürnberg

Lukas Heger

University Hospital Erlangen

Friedrich Paulsen

Friedrich-Alexander-University Erlangen-Nürnberg

Friederike Zunke

University Hospital Erlangen

Philipp Arnold (✉ Philipp.Arnold@fau.de)

Friedrich-Alexander-University Erlangen-Nürnberg

Article

Keywords: COVID-19, SARS-CoV-2, B.1.427/B.1.429, B.1.617.2, B.1.617.1, B.1.1.529, epsilon variant, delta variant, kappa variant, omicron variant, VOC, spike protein, receptor-binding domain, ACE2, receptor interface, molecular dynamics simulations

Posted Date: January 12th, 2022

DOI: <https://doi.org/10.21203/rs.3.rs-1228784/v1>

License:   This work is licensed under a Creative Commons Attribution 4.0 International License.

[Read Full License](#)

Version of Record: A version of this preprint was published at Computational and Structural Biotechnology Journal on February 1st, 2022. See the published version at <https://doi.org/10.1016/j.csbj.2022.02.015>.

1 **Molecular dynamics simulations of the**
2 **delta and omicron SARS-CoV-2 spike – ACE2 complexes**
3 **reveal distinct changes between both variants**

4
5 Eileen Socher^{1,2}, Lukas Heger³, Friedrich Paulsen^{1,4}, Friederike Zunke⁵ and
6 Philipp Arnold¹

7 ¹Institute of Anatomy, Functional and Clinical Anatomy, Friedrich-Alexander University Erlangen-Nürnberg (FAU), Erlangen, Germany; eileen.socher@fau.de (E.S.); friedrich.paulsen@fau.de (F.P.); philipp.arnold@fau.de (P.A.)

10 ²Institute for Clinical and Molecular Virology, Friedrich-Alexander University Erlangen-Nürnberg (FAU),
11 University Hospital Erlangen, Erlangen, Germany; eileen.socher@fau.de

12 ³Laboratory of Dendritic Cell Biology, Department of Dermatology, Friedrich-Alexander University Erlangen-Nürnberg (FAU), University Hospital Erlangen, Erlangen, Germany; lukas.heger@uk-erlangen.de

15 ⁴Sechenov University, Department of Operative Surgery and Topographic Anatomy, 119992 Moscow, Russia; friedrich.paulsen@fau.de

17 ⁵Department of Molecular Neurology, University Hospital Erlangen, Friedrich-Alexander University Erlangen-Nürnberg (FAU), Erlangen, Germany; friederike.zunke@fau.de

19 *Correspondence: eileen.socher@fau.de (E.S.) and philipp.arnold@fau.de (P.A.);

21 **Keywords:** COVID-19, SARS-CoV-2, B.1.427/B.1.429, B.1.617.2, B.1.617.1, B.1.1.529, epsilon variant,
22 delta variant, kappa variant, omicron variant, VOC, spike protein, receptor-binding domain, ACE2, receptor interface, molecular dynamics simulations

25 **Abstract**

26 SARS-CoV-2, the virus which causes the COVID-19 pandemic, changes frequently through the appear-
27 ance of mutations constantly leading to new variants. However, only few variants evolve as dominating
28 and will be considered as “Variants of Concern” (VOCs) by the world health organization (WHO). At the
29 end of 2020 the alpha (B.1.1.7) variant appeared in the United Kingdom and dominated the pandemic
30 situation until mid of 2021 when it was substituted by the delta variant (B.1.617.2) that first appeared
31 in India as predominant variant. At the end of 2021, SARS-CoV-2 omicron (B.1.1.529) evolved as the
32 dominating variant. Here, we use *in silico* modeling and molecular dynamics (MD) simulations of the
33 receptor-binding domain of the viral spike protein and the host cell surface receptor ACE2 to analyze
34 and compare the interaction pattern between the wild type, delta and omicron variants. We identified
35 residue 493 in delta (glutamine) and omicron (arginine) with altered binding properties towards ACE2.

36 **Introduction**

37 The COVID-19 pandemic caused by the novel severe acute respiratory syndrome coronavirus 2 (SARS-
38 CoV-2) is driven by newly emerging variants that arise from the original virus. Although most of the
39 genetic changes have little to no impact on the virus’ properties, some virus variants arise with higher
40 transmissibility and/or increased virulence. These variants are classified as “*Variants of Concern*” (VOC)
41 by the WHO. In January 2022, the WHO listed five VOCs labeled with Greek letters¹: (1) the alpha var-
42 iant (Pango lineage: B.1.1.7) that emerged in the United Kingdom, (2) the beta variant (Pango lineage:
43 B.1.351) from South Africa, (3) the gamma variant (Pango lineage: P.1) from Brazil, (4) the delta variant
44 (Pango lineage: B.1.617.2) first detected in India and the omicron variant (Pango lineage: B.1.1.529)
45 first identified in South Africa in November 2021².

46 All these VOCs listed by the WHO acquired some distinctive mutations (Fig. 1a lists the mutations of
47 the predominant delta and omicron variants) in the trimeric spike glycoprotein of SARS-CoV-2, which
48 specifically binds with its receptor-binding domain (RBD) to the host cell receptor angiotensin-convert-
49 ing enzyme 2 (ACE2)³⁻⁵. This binding step is crucial for viral entry into a host cell to initiate infection
50 (Fig. 1b)^{6,7}. Therefore, understanding the interaction of the virus with ACE2 at the cell surface is fun-
51 damentally important in the fight against SARS-CoV-2. The protein structure of the RBD of the wild
52 type spike protein in complex with ACE2 is known (e.g. PDB ID code: 7KMB⁸) and allows characteriza-
53 tion of receptor binding at the atomic level, greatly improving our understanding of host-pathogen
54 interactions at this site. By introducing the observed mutations into the wild type RBD–ACE2 complex
55 structure with *in silico* modeling and subsequently conducting molecular dynamics (MD) simulations
56 of these RBD–ACE2 complexes, the influence of specific mutations in the RBD on binding towards the
57 human receptor can be strongly enhanced⁹⁻¹¹. Experimentally determined protein structures provide
58 the basis for MD simulations, which can add information on the protein dynamics, the flexibility and
59 residue interactions that would be difficult to access with experimental methods. Additionally, MD
60 simulations can today often be performed and analyzed much faster than experimentally determined
61 structures can be obtained and therefore it can serve as a predictive tool.

62 The mentioned alpha, beta, gamma and omicron variants harbor as common feature all a substitution
63 of asparagine-to-tyrosine at position 501 (N501Y) in the RBD, which is not present in the delta variant¹².
64 In addition to the N510Y mutation, omicron carries 14 other mutations within the RBD (Fig. 1a). A
65 considerable number of them can be found at the direct binding interface with ACE2 (Fig. 1b). In con-
66 trast to omicron, the delta variant has a characteristic leucine-to-arginine substitution at position 452
67 (L452R), which was also earlier detected in the related kappa variant (B.1.617.1) and in an unrelated
68 lineage in the United States of America (epsilon variant: B.1.427/B.1.429). For variants carrying this
69 L452R mutation, stronger affinity of the spike protein for the ACE2 receptor was described^{13,14}. The

70 delta and omicron variants share a common T478K mutation and for delta reduced affinity of neutral-
71 izing antibodies at this position was shown¹⁵⁻¹⁷. In omicron many of the mutations found at the RBD
72 are located within epitopes recognized by neutralizing antibodies. An exemplary array of such neutral-
73 izing antibodies is shown in Supplementary Fig. 1 and experimental data suggests reduced binding of
74 antibodies from patient sera^{18,19}. Of note, especially antibodies binding at the RBD at the site of contact
75 formation with ACE2 show high neutralization properties²⁰.

76 The present study compares the original wild type (wt), the delta variant and the similar variants epsi-
77 lon and kappa with the omicron variant. We identify residue 493 within the RBD as a major difference
78 between all three variants. In wt and delta residue 493 is a glutamine (Gln493) and we show that the
79 delta variant amino acid exchange L452R induces a rearrangement in all three L452R carrying variants
80 (epsilon, delta and kappa) that increase the number of contacts and the number of hydrogen bonds
81 with ACE2 for Gln493. The omicron variant expresses an arginine at position 493 and this arginine
82 forms very stable salt bridges with residues glutamate 35 (Glu35) and aspartate 38 (Asp38) of the host
83 cell receptor ACE2. In previous reports²¹ an exchange from glutamine to lysine was reported at position
84 493 and we can show, that the omicron variants with Q493R or Q493K show very similar changes in
85 contact formation with ACE2. However, for Q493R we also identified salt bridge formation with aspar-
86 tate 30 (Asp30) that was not observed for the Q493K mutation. Additionally, omicron also carries an
87 amino acid exchange from lysine 417 to asparagine (K417N). The same mutation was already observed
88 in the beta variant, while in the gamma variant lysine 417 is mutated to a threonine (K417T). In wild
89 type, Lysine 417 forms a very stable salt bridge with aspartate 30 from the ACE2 receptor and we could
90 show that exchange to asparagine or threonine largely disrupts binding at this position⁹.

91 Here, we show that major changes in interaction with ACE2 occur at positions 417, 493, 501 and at
92 position 505 where a tyrosine is mutated to a histidine (Y505H). We also show, that many of the re-
93 maining amino acid exchanges occurring at the interface to ACE2 do not largely influence binding to
94 ACE2, but rather change epitopes for neutralizing antibodies²⁰, which might explain the reduced neu-
95 tralization capacity identified for serum samples from vaccinated patients¹⁸.

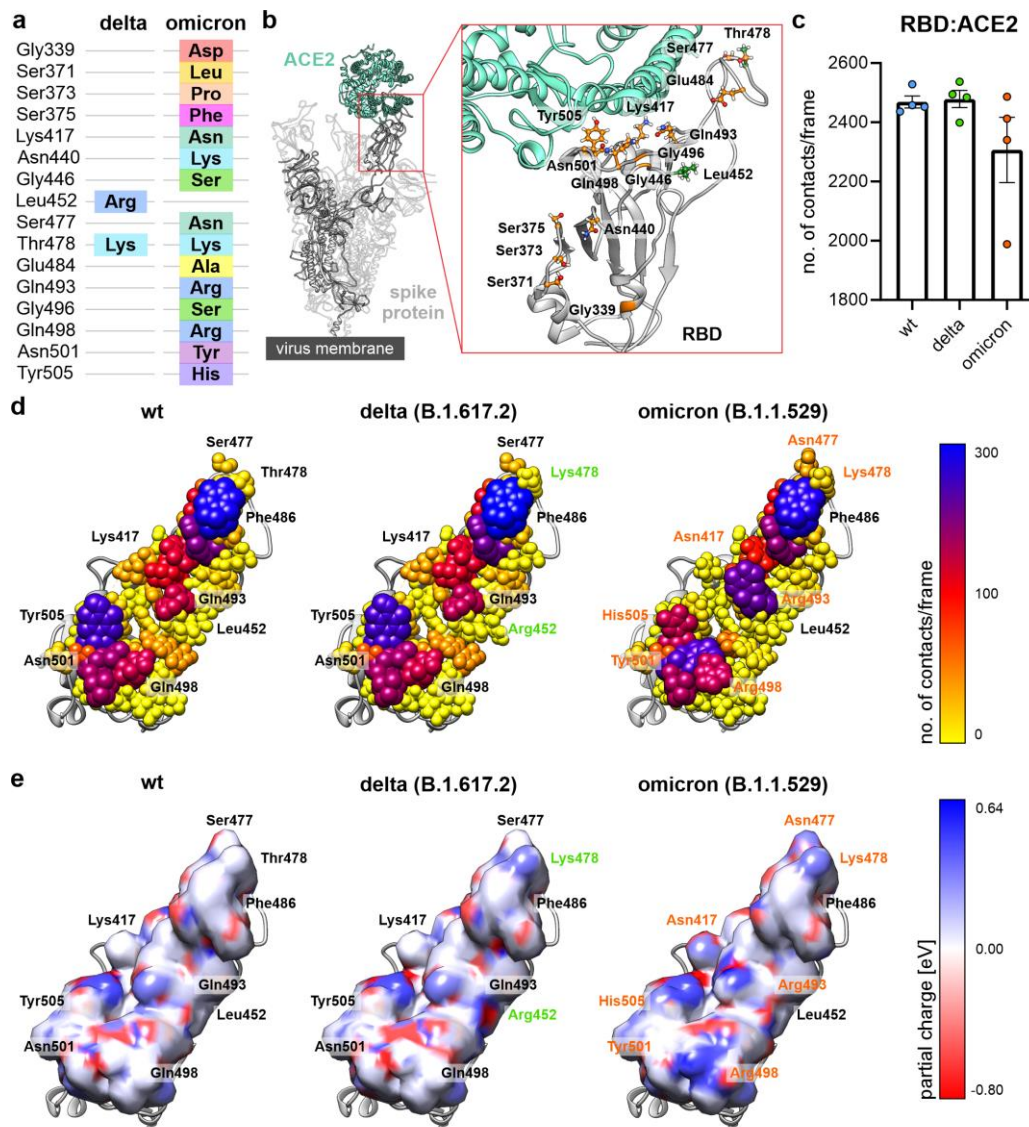
96 **Results**

97 **The contact analyses and electrostatic potential of the viral receptor-binding domain**

98 The SARS-CoV-2 delta and omicron variants have both acquired a threonine-to-leucine (T478K) substi-
99 tution in the RBD. The delta variant carries an additional leucine-to-arginine (L452R) substitution in the
100 RBD and the omicron variant has, in addition to this T478K mutation, 14 other mutations within the
101 RBD (Fig. 1a). In order to compare individual virus variants, we performed four independent MD sim-
102 ulation runs over 500 ns for every variant's RBD in complex with ACE2. Subsequently, we analyzed the
103 overall intermolecular contacts formed between the human ACE2 and the viral RBD of the wild type
104 and the delta and omicron variants. We found a reduced number of contacts between the RBD and
105 ACE2 for the omicron variant, while the number of contacts for the delta variant was not markedly
106 changed (Fig. 1c). Then, we assigned the individual number of contacts to all RBD amino acids within
107 8 Å distance to ACE2 and found marked differences for residues 493, 501 and 505 (Fig. 1d, Supplemen-
108 tary Fig. 1a). Wild type and delta variant express an asparagine at position 501, whereas the omicron
109 variant harbors a tyrosine (N501Y) at this position. The functional consequences of this N501Y muta-
110 tion were already described²² and a cryo-electron microscopy structure carrying this N501Y exchange
111 in complex with ACE2 was also experimentally solved (PDB ID code: 7MJN²³). In the omicron variant,
112 the tyrosine at position 505 (wt and delta variant) is mutated to histidine and we identified a reduced
113 number of contacts to ACE2 for histidine at this position (Fig. 1d, Supplementary Fig. 2a and Supple-
114 mentary Fig. 2b). In detail, residue 505 interacts with the carbon atoms of the side chain of lysine 353
115 on ACE2 (Supplementary Fig. 2c). Here a pi-electron ring system (as for tyrosine expressing variants)

116 might have more contacts than the inserted histidine in omicron. For the epsilon (B.1.427/B.1.429) and
 117 kappa (B.1.617.1) variant, we also performed contact analyses and found no marked differences on
 118 the individual amino acid level (Supplementary Fig. 2d). As the omicron variant shows a considerable
 119 number of positively charged amino acids at sites of mutation, we analyzed the electrostatic potential
 120 at the RBD-ACE2 interface and found increased electro positivity in the delta variant (L452R and T478K)
 121 and even more pronounced in the omicron variant (T478K, Q493R, Q498R and Y505H; Fig. 1e). How-
 122 ever, the omicron variant also loses a positively charged amino acid at the interaction interface at
 123 position 417 (K417N; Fig. 1b, Fig. 1e).

124

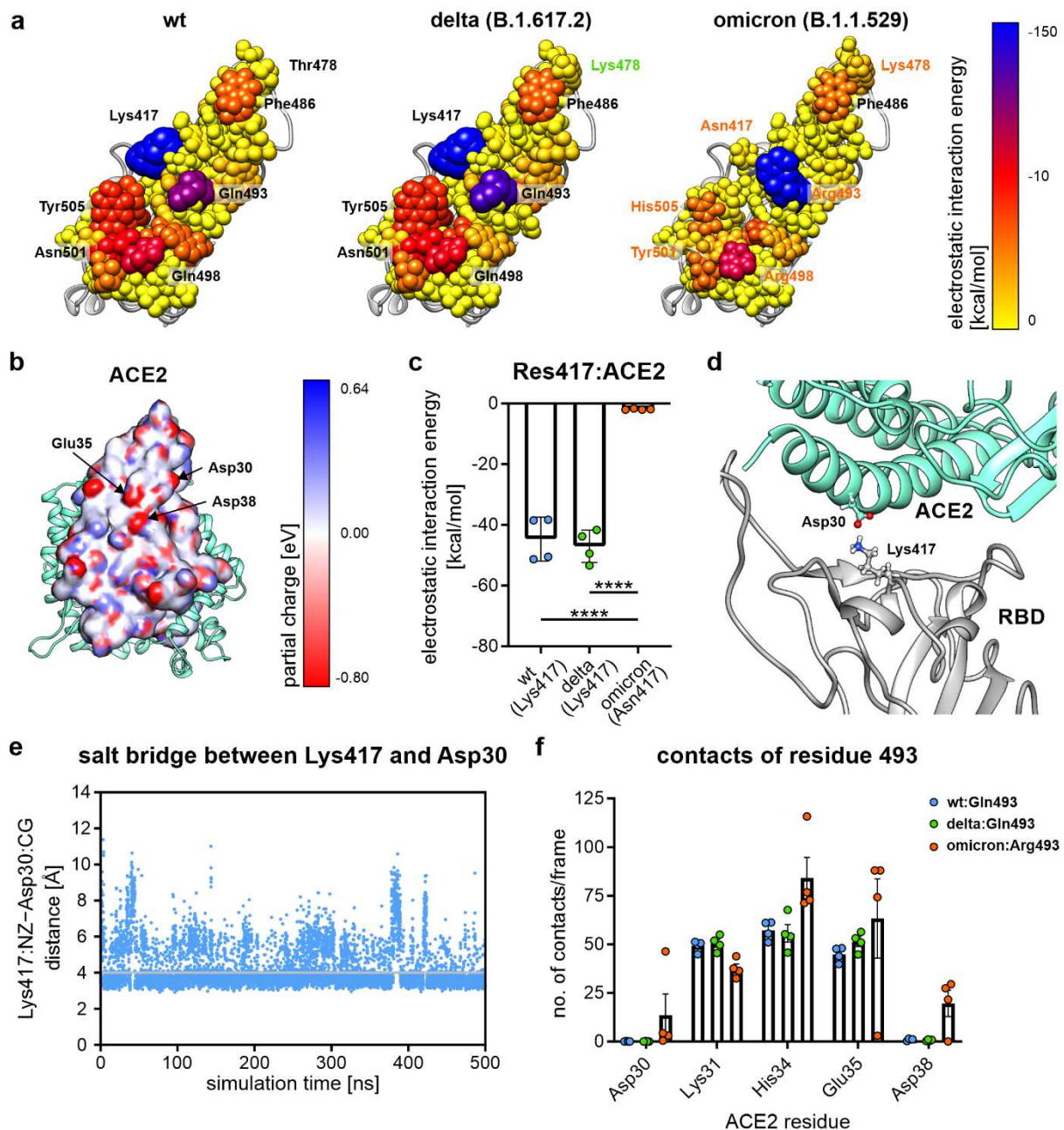


125
 126 **Figure 1: Number of contacts and electrostatic potential.** **a**, Amino acid exchanges at distinct positions in the
 127 delta and omicron variants. **b**, Structural representation of the SARS-CoV-2 spike protein on the viral membrane
 128 with the inset showing all residues mutated in delta (B.1.617.2, green) or omicron (B.1.1.529, orange). **c**, Number
 129 of contacts between the RBD and ACE2 for wt, delta and omicron. **d**, Structural representation of the interface
 130 of the RBD with ACE2 according to the number of contacts in color code. Residues with a green label are mutated
 131 in the delta variant and residues with an orange label are mutated in omicron. **e**, Surface representation of the
 132 interface formed by the RBD with ACE2. Surface coloring according to the electrostatic potential of the underlying
 133 residues with 0.64 eV in blue and -0.80 eV in red.

134 **The interaction between residue 493 and ACE2 is altered in delta and omicron variant**

135 As numerous positively charged amino acids appear at the interaction interface, we also analyzed the
136 linear electrostatic interaction energy to identify newly formed or resolved intermolecular salt bridges.
137 Largest differences between wt, delta and omicron were found at positions 417 and 493 (Fig. 2a, Sup-
138 plementary Fig. 3). Analyzing the electrostatic potential at the interaction interface on ACE2 revealed
139 aspartate 30, glutamate 35 and aspartate 38 as potential interaction partners for these two residues.
140 For other variants that exchanged lysine 417 to asparagine or threonine, we already identified a
141 strongly reduced electrostatic interaction energy with aspartate 30⁹. Thus it was not very surprising
142 that we found the same reduction for the omicron variant (Fig. 2c) and a salt bridge in wt (Fig. 2d) that
143 also remains stable over time (Fig. 2e). Next, we analyzed contact formation for residue 493 (Fig. 2f).
144 We found that wt and delta (both with Gln493) behave similar, but that omicron shows some major
145 differences. The delta variant shows a small increase in contact formation with lysine 31 and glutamate
146 35 (Fig. 2f). In contrast, omicron changes its interaction profile completely. For one MD simulation run
147 we identified interaction with aspartate 30 (Asp30) and in three runs increased interaction with gluta-
148 mate 35 (Glu35) and with aspartate 38 (Asp38). Additionally, the interaction with lysine 31 (Lys31) is
149 reduced in all four simulation runs of the omicron variant (Fig. 2f) probably due to electrostatic repul-
150 sion between the positively charged arginine 493 and the also positively charged lysine 31.

151



152

153 **Figure 2: Linear electrostatic interaction shows two major changes in omicron.** **a**, Structural representation of
 154 the RBD interface with ACE2 with residues shown as spheres with their size and color according to their electro-
 155 static interaction. **b**, Surface representation of the binding interface of ACE2 with the RBD. Surface color is labeled
 156 according to the partial charge of the underlying residues with the three negatively charged residues aspartate
 157 30 (Asp30), glutamate 35 (Glu35) and aspartate 38 (Asp38). **c**, Linear electrostatic binding energy of residue 417
 158 in wt (blue), delta (green) and omicron (orange; **** p<0.0001 one-way ANOVA). **d**, Structural representation
 159 of the salt bridge formed by lysine 417 (Lys417) from the RBD and aspartate 30 (Asp30) from ACE2 in the wt
 160 complex. **e**, Time resolved distance plot of the distance between side chain atoms of Lys417 and Asp30 in the wt
 161 complex. **f**, Number of contacts per frame formed by residue 493 with interacting ACE2 residues.

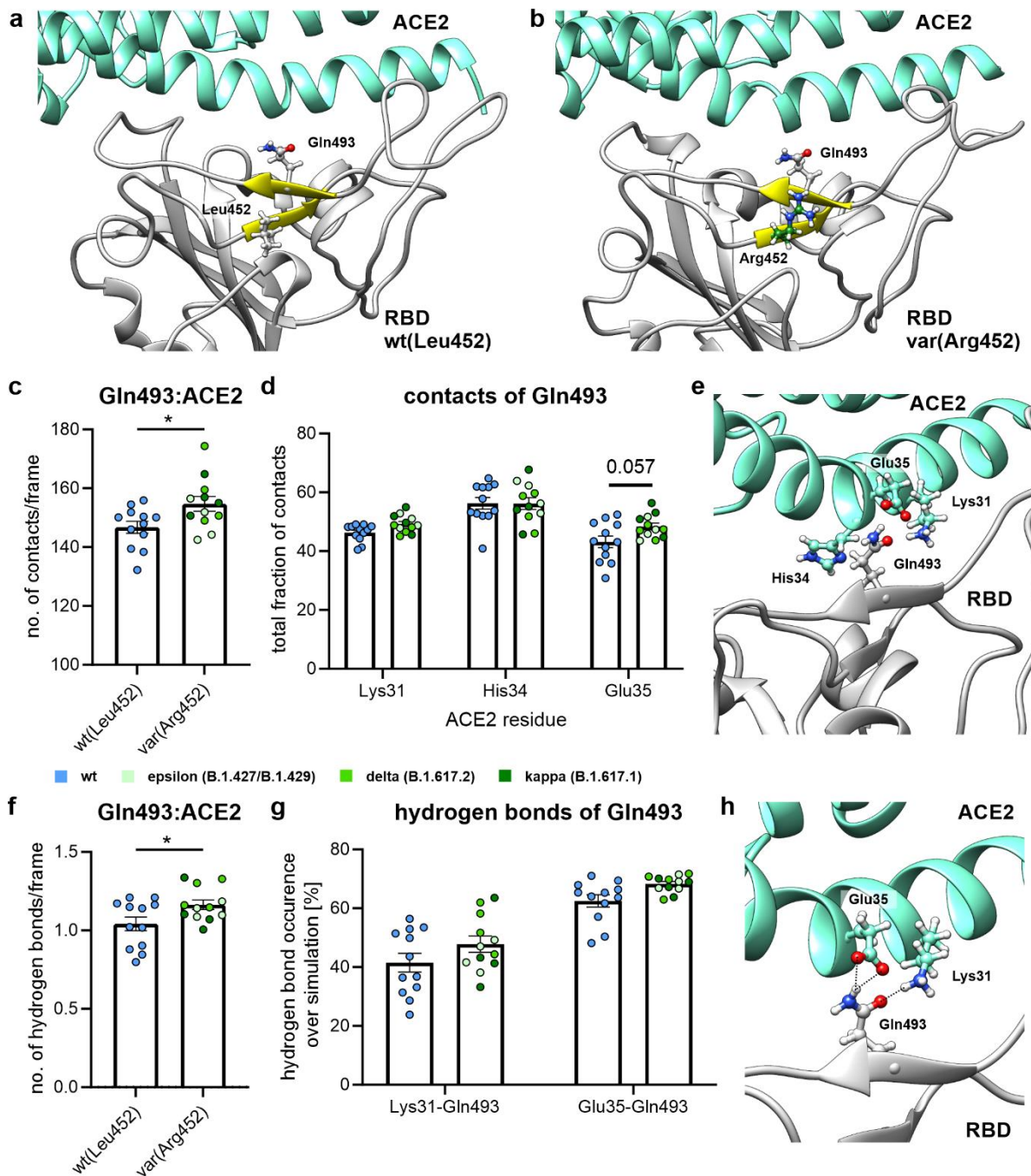
162

163 The delta variant shows increased hydrogen bond formation with ACE2

164 To analyze changes in the delta variant, we pooled it with four individual MD simulation runs of the
 165 epsilon and four runs of the kappa variant (all these variants carry the L452R mutation) and compared

166 it to twelve 500 ns long simulation runs of the wt RBD-ACE2 complex (eight of them were already de-
167 scribed earlier^{9,10}). Within the neighboring beta sheet of glutamine 493, the L452R exchange can be
168 found (Fig. 3a, b), thereby changing the structural environment of glutamine 493. We found that the
169 number of intermolecular contacts between glutamine 493 and the human receptor ACE2 increases in
170 the different L452R variants compared to wild type RBD-ACE2 complexes (Fig. 3c). Decomposed on
171 the individual amino acid level, although not significant, we identified the ACE2 residues glutamate 35
172 and to a minor extend lysine 31 with an increased number of contacts to glutamine 493 (Fig. 3d,e).
173 Contact formation between glutamine 493 and histidine 34 of ACE2 was unchanged, however (Fig.
174 3d,e). As glutamine residues engage in hydrogen bonds, we also analyzed the number of intermolecu-
175 lar hydrogen bonds of glutamine 493 with ACE2 and found a significant increase for variants that ex-
176 press the L452R mutation (Fig. 3f). Detailed analysis showed an increased occurrence of hydrogen
177 bonds with lysine 31 and with glutamate 35 (Fig. 3g). The structural representation illustrates that the
178 side chain oxygen atom of glutamine 493 forms a hydrogen bond with the side chain of lysine 31 from
179 ACE2 while one of the hydrogens of the amino group forms hydrogen bonds with the oxygen atoms of
180 the carboxyl group of glutamate 35 (Fig. 3h). A detailed root-mean-square fluctuation (RMSF) analysis
181 (Supplementary Fig. 4a) showed a reduced flexibility for the entire glutamine 493 (Supplementary Fig.
182 4b) and especially for side chain atoms of the amino group (NE2, HE21 and HE22; Supplementary Fig.
183 4b) in the different L452R variants compared to wild type RBD-ACE2 complexes. This reduced flexibility
184 of glutamine's side chain atoms can be observed due to the stronger hydrogen bond network of glu-
185 tamine 493 with ACE2, which stabilizes the side chain position. Histidine 34 does not form hydrogen
186 bonds with glutamine 493, but forms a hydrogen bond with tyrosine 453 (Supplementary Fig. 4c,d).
187 Together, we can conclude that the delta variant shows an increase in contacts and consequently in
188 hydrogen bond formation of glutamine 493 with ACE2 and that this might contribute to an increased
189 binding.

190



191

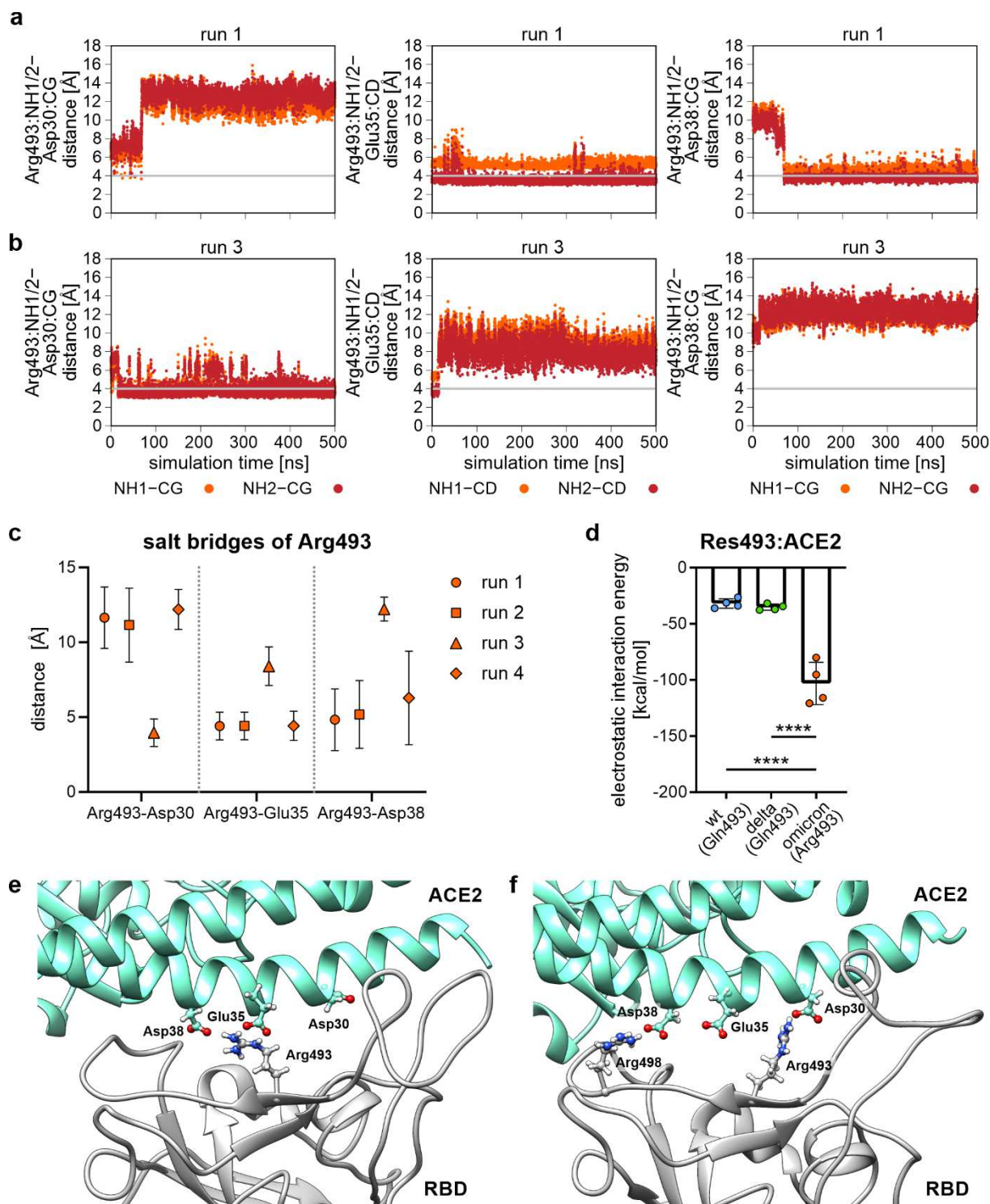
192 **Figure 3: Hydrogen bond rearrangement in delta.** **a**, Structural representation of the glutamine 493 (Gln493)
 193 and leucine 452 (Leu452) as expressed on two neighboring β -strands forming a small 2-stranded antiparallel β -
 194 sheet (yellow) in wt. **b**, As in figure panel **a**, but with residue 452 exchanged to arginine (Arg452, green) as ex-
 195 pressed on delta (medium green), epsilon (light green) and kappa (dark green) variants. **c**, Combined analysis of
 196 wt and three variants that carry the leucine 452 arginine (L452R) exchange with regard to the number of contacts
 197 formed by glutamine 493 (Gln493) with ACE2 (* p<0.05, two-tailed Student's T-test). **d**, Residue specific
 198 analysis of the number of contacts between wt and L452R expressing variants (one-way ANOVA). **e**, Structural repre-
 199 sentation of glutamine 493 (Gln493) expressed on the RBD and its interaction partners from ACE2 lysine 31 (Lys31),
 200 histidine 34 (His34) and glutamate 35 (Glu35). **f**, Number of hydrogen bonds formed by glutamine 493 (Gln493)
 201 per frame comparing wt and L452R expressing variants (* p<0.05, two-tailed Student's T-test). **g**, Hydrogen bond
 202 formation between glutamine 493 (Gln493) from the RBD and lysine 31 (Lys31) and glutamate 35 (Glu35, both
 203 ACE2). **h**, Structural representation of the hydrogen bonds formed between glutamine 493 (Gln493, RBD) and
 204 lysine 31 (Lys31, ACE2) and glutamate 35 (Glu35, ACE2).

205

206 **The omicron variant forms two new stable salt bridges with ACE2 residues**

207 As described above (Fig. 2f), we identified an entirely altered interaction pattern for arginine at posi-
208 tion 493. The number of contacts with glutamate 35 increased and contacts with aspartate 38 were
209 newly formed and not present in residues expressing a glutamine at position 493 (Fig. 2f). For three of
210 our MD simulations, these two newly formed salt bridges can also be appreciated in time course dis-
211 tance plots of arginine 493 with aspartate 30, glutamate 35 and aspartate 38 (Fig. 4a; Supplementary
212 Fig. 5a). However, one of our MD simulation runs showed a different picture and we found a stable
213 intermolecular salt bridge between arginine 493 and aspartate 30 on ACE2 (Fig. 4b). Analyzing the
214 average distances to favored residues on ACE2 within single runs provided insight into the stability of
215 the individual salt bridges (Fig. 4c). Especially interactions between arginine 493 and aspartate 30 and
216 glutamate 35 show low standard deviations with average distances below 5 Å, thus strongly supporting
217 ionic interaction. Analysis of the linear electrostatic interaction energy at position 493 showed a strong
218 increase for omicron when compared to wt and delta (Fig. 4d). Thus, we can now postulate two differ-
219 ent interactions with ACE2 for arginine at position 493 in the omicron variant. In the first mode, it
220 forms salt bridges with glutamate 35 and aspartate 38 (Fig. 4e) and in the second mode it forms a salt
221 bridge with aspartate 30 (Fig. 4f). Within the same simulation run, where we identified a stable salt
222 bridge between arginine 493 and aspartate 30 from ACE2, we also identified a stable salt bridge be-
223 tween arginine 498 (only present in omicron) and aspartate 38 (Fig. 4f, Supplementary Fig. 5b). To-
224 gether, omicron carrying an arginine at position 493 (Q493R) shows a higher flexibility in contact for-
225 mation than wt or delta in the same region. As there was a sequence conflict at position 493 at the
226 beginning, we also simulated the RBD-ACE2 complex with a lysine at this position 493. All runs showed
227 stable salt bridges between lysine 493 and glutamate 35 (Supplementary Fig. 6a,b) and aspartate 38
228 (Supplementary Fig. 6c,d) of ACE2. A lysine side chain at this position might be too short to interact
229 with aspartate 30 (Supplementary Fig. 6e). The increase in linear electrostatic interaction energy, how-
230 ever, remains the similar (Supplementary Fig. 6f). One selection advantage of the omicron over the
231 omicron+Q493K variant might be the more flexible interaction regime at this position.

232



233

234 **Figure 4: Newly formed salt bridges in omicron between arginine 493 and negatively charged residues on ACE2.**

235 **a**, Representative distance plots of arginine 493 (RBD, omicron) and aspartate 30 (Asp30), glutamate 35 (Glu35)

236 and aspartate 38 (Asp38) (all three on ACE2). **b**, Distance plots of a different MD simulation run than shown in

237 figure panel **a** between the same residues. **c**, Average distance with standard deviation error bars shown for four

238 individual 500 ns runs for residues arginine 493 (RBD, omicron) and aspartate 30 (Asp30), glutamate 35 (Glu35)

239 and aspartate 38 (Asp38). **d**, Linear electrostatic interaction energy for residue 493 analyzed for wt (blue), delta

240 (green) and omicron (orange; **** $p < 0.0001$, one-way ANOVA). **e**, Structural representation of the two newly

241 formed salt bridges between arginine 493 (Arg493) on the RBD and glutamate 35 (Glu35) and aspartate 38

242 (Asp38) both expressed on ACE2. **f**, Structural representation of salt bridges formed between Arg493 (RBD) and

243 Asp30 (ACE) and Arg498 (RBD) and Asp38 (ACE2).

244 Discussion

245 The appearance of a L452R exchange within the RBD of the SARS-CoV-2 spike protein rendered the
246 affected variants to former “Variants under Investigation” (epsilon, kappa) or current “Variant of Con-
247 cern” (delta variant)¹. The delta variant dominated the pandemic worldwide from mid-2021. All three
248 variants carry additional amino acid exchanges within the other parts of the spike protein, including
249 the D614G variant that we identified as a potential molecular switch to liberate the fusion peptide¹⁰.
250 Here we show, that the L452R mutation induces an increased number of hydrogen bonds formed by
251 glutamine 493 between the RDB (delta variant) and ACE2. This increase, might induce a stronger inter-
252 action between both and support increased viral infectivity. Comparing the omicron variant to wt and
253 delta reveals major differences in RBD-ACE2 interaction. As in the alpha variant, omicron carries a
254 N501Y mutation and, as the beta variant, carries the K417N mutation. The N501Y mutation apparently
255 increases the binding energy between RBD and ACE2 and the K417N mutation reduces it²². Before
256 delta dominated the pandemic starting mid-2021, the alpha variant outcompeted the wt SARS-CoV-2
257 variant end of 2020/beginning of 2021. Parallel with the alpha variant, the beta and gamma variants
258 appeared both with exchanges for lysine at position 417 that induced a loss of the salt bridge at this
259 position⁹. In omicron this salt bridge is also lost. However, through the exchange of glutamine 493 to
260 an arginine (Q493R), two additional salt bridges are formed (either by arginine 493 itself or by arginine
261 498) and a strong increase in linear electrostatic interaction energy can be observed. The variability in
262 salt bridge formation at positions 493 and 498 might increase the probability for RBD-ACE2 interaction
263 and thereby increase infectivity. As a side note, we could also show that a lysine at this position has a
264 less flexible interaction pattern. Overall, three mutations within the RBD of omicron can be attributed
265 to direct changes in interaction with ACE2 and these are K417N, Q493R and N501Y. With the exchange
266 of tyrosine 505 to histidine, a reduced number of contacts is associated. However, the effect of this
267 exchange cannot be fully judged. When comparing the delta and omicron variant to wt an additional
268 trend becomes evident. Amino acid exchanges within the RBD render it more electropositive. Delta is
269 more positive than wt and omicron more positive than delta. This might enable a better passive adhe-
270 sion to the negatively charged glycolcalyx and here especially to heparin sulfate, which is a critical
271 factor for SARS-CoV-2 binding²⁴⁻²⁶. Thus, we can identify amino acid exchanges which (i) influence di-
272 rect interaction with ACE2, (ii) change epitopes of neutralizing antibodies and/or (iii) change the elec-
273 trostatic surface potential. In omicron, five of the fifteen mutations within the RBD insert positively
274 charged amino acids (N440K, T478K, Q493R, Q498R and Y505H) and only one is lost (K417N). All of
275 these six positions are within epitope regions for neutralizing antibodies²⁰. In conclusion, omicron
276 started to dominate the pandemic at the end of 2021 with patient numbers rising steeply in affected
277 areas. MD simulation and structural analysis of the RBD-ACE2 complex shows clear differences of omi-
278 cron to the delta variant. Omicron has progressed in terms of ACE2 binding, in terms of immune escape
279 and presents a more positively charged interface area.

280

281 Methods

282 Generation of the starting structures

283 To investigate the interface between the RBD of the spike protein and ACE2, the respective wild type
284 start structure was taken from the PDB database (PDB ID code: 7KMB (10.1016/j.chom.2020.11.004)).
285 To also generate the starting structures for the MD simulations of the different SARS-CoV-2 variants,
286 the amino acid substitutions (epsilon spike variant (B.1.427/B.1.429): L452R; delta variant (B.1.617.2):
287 L452R and T478K; kappa variant (B.1.617.1): L452R and E484Q, omicron variant (B.1.1.529): G339D,
288 S371L, S373P, S375F, K417N, N440K, G446S, S477N, T478K, E484A, Q493R, G496S, Q498R, N501Y,
289 Y505H and for an omicron variant with a lysine at position 493: G339D, S371L, S373P, S375F, K417N,

290 N440K, G446S, S477N, T478K, E484A, Q493K, G496S, Q498R, N501Y, Y505H) were introduced with
291 Swiss-PdbViewer 4.1.0²⁷ (<http://www.expasy.org/spdbv/>).

292 For the electrostatic analyses of the protein surface, “PQR” output files were generated by using charge
293 parameters assigned with the APBS-PDB2PQR software suite²⁸ (<https://server.poissonboltzmann.org/>).
294

295 **Molecular dynamics simulations**

296 Molecular dynamics simulations were performed exactly as described before^{9,10}. By using version 20
297 of the Amber Molecular Dynamics software package (ambermd.org)²⁹, the ff14SB force field³⁰ and the
298 Amber Tool LEaP, all systems were electrically neutralized with Na⁺ ions and solvated with TIP3P³¹ wa-
299 ter molecules. The receptor-binding domain complexed with ACE2 was solvated in a water box with
300 the shape of a truncated octahedron and a distance of at least 25 Å from the borders to the solute.

301 Minimization was carried out in three consecutive parts to optimize the geometry of the initial struc-
302 tures. In the first minimization part, all water molecules were minimized, while all other atoms were
303 restrained at the initial positions by using a constant force of 10 kcal·mol⁻¹·Å⁻². During the second part,
304 additional relaxation of the sodium ions and the hydrogen atoms of the protein was allowed, while the
305 remaining protein was restrained with 10 kcal·mol⁻¹·Å⁻². In the third part, the entire protein, ions, and
306 water molecules were minimized without any restraints. All three minimization parts started with 2500
307 steps using the steepest descent algorithm, followed by 2500 steps of a conjugate gradient minimiza-
308 tion. After minimization, the systems were equilibrated in two successive steps. In the first step, the
309 temperature was increased from 10 to 310 K within 0.1 ns and the protein was restrained with a con-
310 stant force of 5 kcal·mol⁻¹·Å⁻². In the second step (0.4 ns length), only the C_α atoms of the protein were
311 restrained with a constant force of 5 kcal·mol⁻¹·Å⁻². In both equilibration steps, the time step was 2 fs.
312 Minimization and equilibration were carried out on CPUs, while the subsequent production runs were
313 performed using pmemd.CUDA on Nvidia A100 GPUs³²⁻³⁴. Subsequent 500 ns long production runs
314 were performed without any restraints and at 310 K (regulated by a Berendsen thermostat³⁵). Further-
315 more, the constant pressure periodic boundary conditions with an average pressure of 1 bar and iso-
316 tropic position scaling were used. For bonds involving hydrogen, the SHAKE algorithm³⁶ was applied in
317 the equilibration and production phases. To accelerate the production phase of the MD simulations,
318 hydrogen mass repartitioning (HMR)³⁷ was used in combination with a time step of 4 fs. For statistical
319 analyses, four independent 500 ns long MD simulation runs were performed for the epsilon, delta,
320 kappa and omicron spike protein RBD variants in complex with ACE2. For the wild type RBD in complex
321 with ACE216 independent 500 ns long MD simulation runs were used (eight completely new MD sim-
322 ulations and in addition also eight MD simulation runs conducted for two earlier studies^{9,10} were re-
323 evaluated).

324 Trajectory analysis (analysis of root-mean-square fluctuations (RMSF), analysis of contacts (always with
325 distance criterion of ≤5 Å between any pair of atoms; total fraction of contacts for residue pairs), meas-
326 urement of interatomic distances, calculation of electrostatic linear interaction energy and hydrogen
327 bond analyses were performed using the Amber tool cpptraj³⁸.

328 **Statistics and display**

329 Statistical analyses were performed with GraphPad Prism (version 9.2.0 for Windows, GraphPad Soft-
330 ware, San Diego, California USA, www.graphpad.com) and statistical tests were applied as indicated
331 below the figure. Plots were created in GraphPad and all structure images were made with UCSF Chi-
332 mera 1.15³⁹.

333

334 **Acknowledgments**

335 The authors gratefully acknowledge the compute resources and support provided by the Erlangen Re-
336 gional Computing Center (RRZE) and by NHR@FAU. Supported by the Interdisciplinary Center for Clin-
337 ical Research (IZKF) at the University Hospital of the University of Erlangen-Nürnberg to F.Z. (Jochen-
338 Kalden funding program N8) and P.A. (ELAN P075).

339

340 **References**

- 341 1. WHO. <https://www.who.int/en/activities/tracking-SARS-CoV-2-variants>. (2022).
- 342 2. Wang, L. & Cheng, G. Sequence analysis of the emerging SARS-CoV-2 variant Omicron in South
343 Africa. *Journal of Medical Virology* n/a.
- 344 3. Hoffmann, M. et al. SARS-CoV-2 Cell Entry Depends on ACE2 and TMPRSS2 and Is Blocked by
345 a Clinically Proven Protease Inhibitor. *Cell* **181**, 271-280 e8 (2020).
- 346 4. Yang, J. et al. Molecular interaction and inhibition of SARS-CoV-2 binding to the ACE2 receptor.
347 *Nat Commun* **11**, 4541 (2020).
- 348 5. Li, W. et al. Angiotensin-converting enzyme 2 is a functional receptor for the SARS coronavirus.
349 *Nature* **426**, 450-4 (2003).
- 350 6. Jackson, C.B., Farzan, M., Chen, B. & Choe, H. Mechanisms of SARS-CoV-2 entry into cells. *Nat*
351 *Rev Mol Cell Biol* **23**, 3-20 (2022).
- 352 7. Zhou, P. et al. A pneumonia outbreak associated with a new coronavirus of probable bat origin.
353 *Nature* **579**, 270-273 (2020).
- 354 8. Zhou, T. et al. Cryo-EM Structures of SARS-CoV-2 Spike without and with ACE2 Reveal a pH-
355 Dependent Switch to Mediate Endosomal Positioning of Receptor-Binding Domains. *Cell Host*
356 *Microbe* **28**, 867-879 e5 (2020).
- 357 9. Socher, E. et al. Computational decomposition reveals reshaping of the SARS-CoV-2-ACE2
358 interface among viral variants expressing the N501Y mutation. *J Cell Biochem* **122**, 1863-1872
359 (2021).
- 360 10. Socher, E. et al. Mutations in the B.1.1.7 SARS-CoV-2 Spike Protein Reduce Receptor-Binding
361 Affinity and Induce a Flexible Link to the Fusion Peptide. *Biomedicines* **9**(2021).
- 362 11. Jawad, B., Adhikari, P., Podgornik, R. & Ching, W.Y. Key Interacting Residues between RBD of
363 SARS-CoV-2 and ACE2 Receptor: Combination of Molecular Dynamics Simulation and Density
364 Functional Calculation. *J Chem Inf Model* **61**, 4425-4441 (2021).
- 365 12. ECDC. <https://www.ecdc.europa.eu/en/covid-19/variants-concern>. (2021).
- 366 13. Khan, M.I. et al. Impact of the Double Mutants on Spike Protein of SARS-CoV-2 B.1.617 Lineage
367 on the Human ACE2 Receptor Binding: A Structural Insight. *Viruses* **13**(2021).
- 368 14. Deng, X. et al. Transmission, infectivity, and antibody neutralization of an emerging SARS-CoV-
369 2 variant in California carrying a L452R spike protein mutation. *medRxiv* (2021).
- 370 15. Wilhelm, A. et al. Antibody-Mediated Neutralization of Authentic SARS-CoV-2 B.1.617 Variants
371 Harboring L452R and T478K/E484Q. *Viruses* **13**(2021).
- 372 16. Focosi, D. & Maggi, F. Neutralising antibody escape of SARS-CoV-2 spike protein: Risk
373 assessment for antibody-based Covid-19 therapeutics and vaccines. *Rev Med Virol* **31**, e2231
374 (2021).
- 375 17. Liu, C. et al. Reduced neutralization of SARS-CoV-2 B.1.617 by vaccine and convalescent serum.
376 *Cell* **184**, 4220-4236.e13 (2021).
- 377 18. Wilhelm, A. et al. Reduced Neutralization of SARS-CoV-2 Omicron Variant by Vaccine Sera and
378 monoclonal antibodies. *medRxiv*, 2021.12.07.21267432 (2021).
- 379 19. Dejnirattisai, W. et al. Reduced neutralisation of SARS-CoV-2 omicron B.1.1.529 variant by
380 post-immunisation serum. *Lancet* (2021).
- 381 20. Dejnirattisai, W. et al. The antigenic anatomy of SARS-CoV-2 receptor binding domain. *Cell* **184**,
382 2183-2200 e22 (2021).

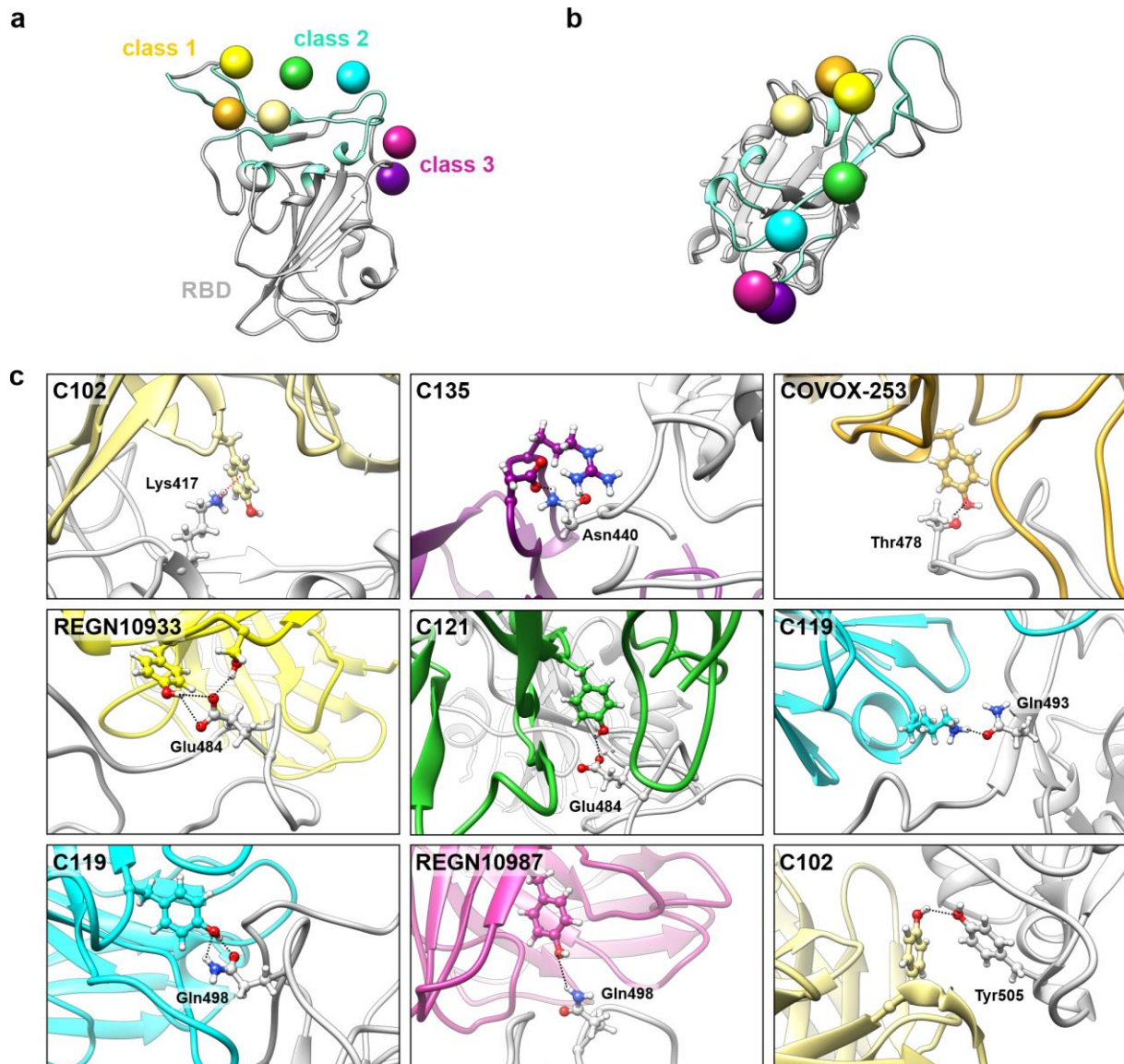
- 383 21. ECDC. Implications of the emergence and spread of the SARS CoV 2 B.1.1. 529 variant of
384 concern (Omicron) for the EU/EEA. (2021).
- 385 22. Starr, T.N. et al. Deep Mutational Scanning of SARS-CoV-2 Receptor Binding Domain Reveals
386 Constraints on Folding and ACE2 Binding. *Cell* **182**, 1295-1310 e20 (2020).
- 387 23. Zhu, X. et al. Cryo-electron microscopy structures of the N501Y SARS-CoV-2 spike protein in
388 complex with ACE2 and 2 potent neutralizing antibodies. *PLoS Biol* **19**, e3001237 (2021).
- 389 24. Wadowski, P.P. et al. Glycocalyx as Possible Limiting Factor in COVID-19. *Front Immunol* **12**,
390 607306 (2021).
- 391 25. Lang, J. et al. Inhibition of SARS pseudovirus cell entry by lactoferrin binding to heparan sulfate
392 proteoglycans. *PLoS One* **6**, e23710 (2011).
- 393 26. Clausen, T.M. et al. SARS-CoV-2 Infection Depends on Cellular Heparan Sulfate and ACE2. *Cell*
394 **183**, 1043-1057 e15 (2020).
- 395 27. Guex, N. & Peitsch, M.C. SWISS-MODEL and the Swiss-PdbViewer: an environment for
396 comparative protein modeling. *Electrophoresis* **18**, 2714-23 (1997).
- 397 28. Jurrus, E. et al. Improvements to the APBS biomolecular solvation software suite. *Protein*
398 *Science* **27**, 112-128 (2018).
- 399 29. Case, D.A. et al. AMBER 2020.
- 400 30. Maier, J.A. et al. ff14SB: Improving the Accuracy of Protein Side Chain and Backbone
401 Parameters from ff99SB. *J Chem Theory Comput* **11**, 3696-713 (2015).
- 402 31. Jorgensen, W.L., Chandrasekhar, J., Madura, J.D., Impey, R.W. & Klein, M.L. Comparison of
403 simple potential functions for simulating liquid water. *The Journal of Chemical Physics* **79**, 926-
404 935 (1983).
- 405 32. Götz, A.W. et al. Routine Microsecond Molecular Dynamics Simulations with AMBER on GPUs.
406 1. Generalized Born. *J Chem Theory Comput* **8**, 1542-1555 (2012).
- 407 33. Salomon-Ferrer, R., Götz, A.W., Poole, D., Le Grand, S. & Walker, R.C. Routine Microsecond
408 Molecular Dynamics Simulations with AMBER on GPUs. 2. Explicit Solvent Particle Mesh Ewald.
409 *J Chem Theory Comput* **9**, 3878-88 (2013).
- 410 34. Le Grand, S., Götz, A.W. & Walker, R.C. SPFP: Speed without compromise—A mixed precision
411 model for GPU accelerated molecular dynamics simulations. *Computer Physics*
412 *Communications* **184**, 374–380 (2013).
- 413 35. Berendsen, H.J.C., Postma, J.P.M., Gunsteren, W.F.v., DiNola, A. & Haak, J.R. Molecular
414 dynamics with coupling to an external bath. *The Journal of Chemical Physics* **81**, 3684-3690
415 (1984).
- 416 36. Jean-Paul Ryckaert, G.C., Herman J.C Berendsen,. Numerical integration of the cartesian
417 equations of motion of a system with constraints: molecular dynamics of n-alkanes. *Journal of*
418 *Computational Physics* **23**, 327-341 (1977).
- 419 37. Hopkins, C.W., Le Grand, S., Walker, R.C. & Roitberg, A.E. Long-Time-Step Molecular Dynamics
420 through Hydrogen Mass Repartitioning. *J Chem Theory Comput* **11**, 1864-74 (2015).
- 421 38. Roe, D.R. & Cheatham, T.E., 3rd. PTRAJ and CPPTRAJ: Software for Processing and Analysis of
422 Molecular Dynamics Trajectory Data. *J Chem Theory Comput* **9**, 3084-95 (2013).
- 423 39. Pettersen, E.F. et al. UCSF Chimera—A visualization system for exploratory research and
424 analysis. *Journal of Computational Chemistry* **25**, 1605-1612 (2004).
- 425 40. Barnes, C.O. et al. SARS-CoV-2 neutralizing antibody structures inform therapeutic strategies.
426 *Nature* **588**, 682-687 (2020).
- 427 41. Hansen, J. et al. Studies in humanized mice and convalescent humans yield a SARS-CoV-2
428 antibody cocktail. *Science* **369**, 1010-1014 (2020).

429

430

431 **Supplementary Figures**

432 **Figure S1:**



433

434 **Figure S1: Neutralizing antibodies from class 1, class 2 and class 3⁴⁰ interact with residues in wild type spike**
 435 **protein which are mutated in the RBD of the delta and/or the omicron variant. a, RBD shown in grey with**
 436 **residues forming the interaction interface with ACE2 highlighted in aquamarine. The colored spheres represent**
 437 **the center of the binding site of the seven exemplarily selected neutralizing antibodies. b, As in figure panel a**
 438 **but structure was rotated to show from a different view. c, Detailed structural representation of RBD interface**
 439 **residues in wild type and the interacting residues of the neutralizing antibodies C102 (PDB ID code: 7K8M)⁴⁰,**
 440 **C135 (PDB ID code:7K8Z)⁴⁰, COVOX-253 (PDB ID code:7BEN)¹⁷, REGN10933 (PDB ID code: 6XDG)⁴¹, C121 (PDB ID**
 441 **code: 7K8Y)⁴⁰, C119 (PDB ID code: 7K8W)⁴⁰ and REGN10987 (PDB ID code: 6XDG)⁴¹ (colors were used as in a).**
 442 **Exemplary structural illustrations are shown only for RBD residues mutated in the delta and/or omicron variants.**
 443 **Dashed lines indicate intermolecular hydrogen bonds or as in the case of Lys417 intermolecular cation-pi inter-**
 444 **actions.**

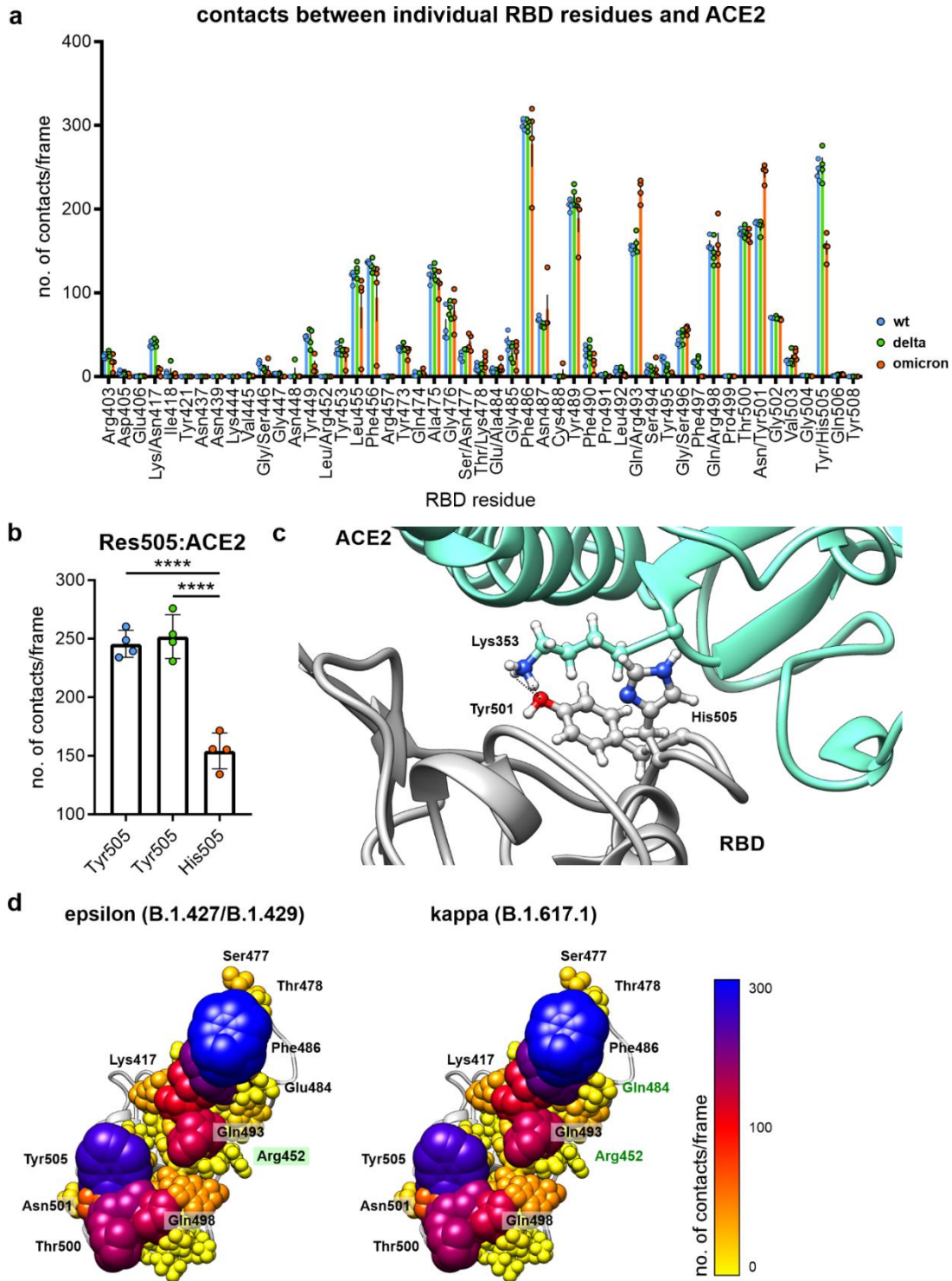
445

446

447

448

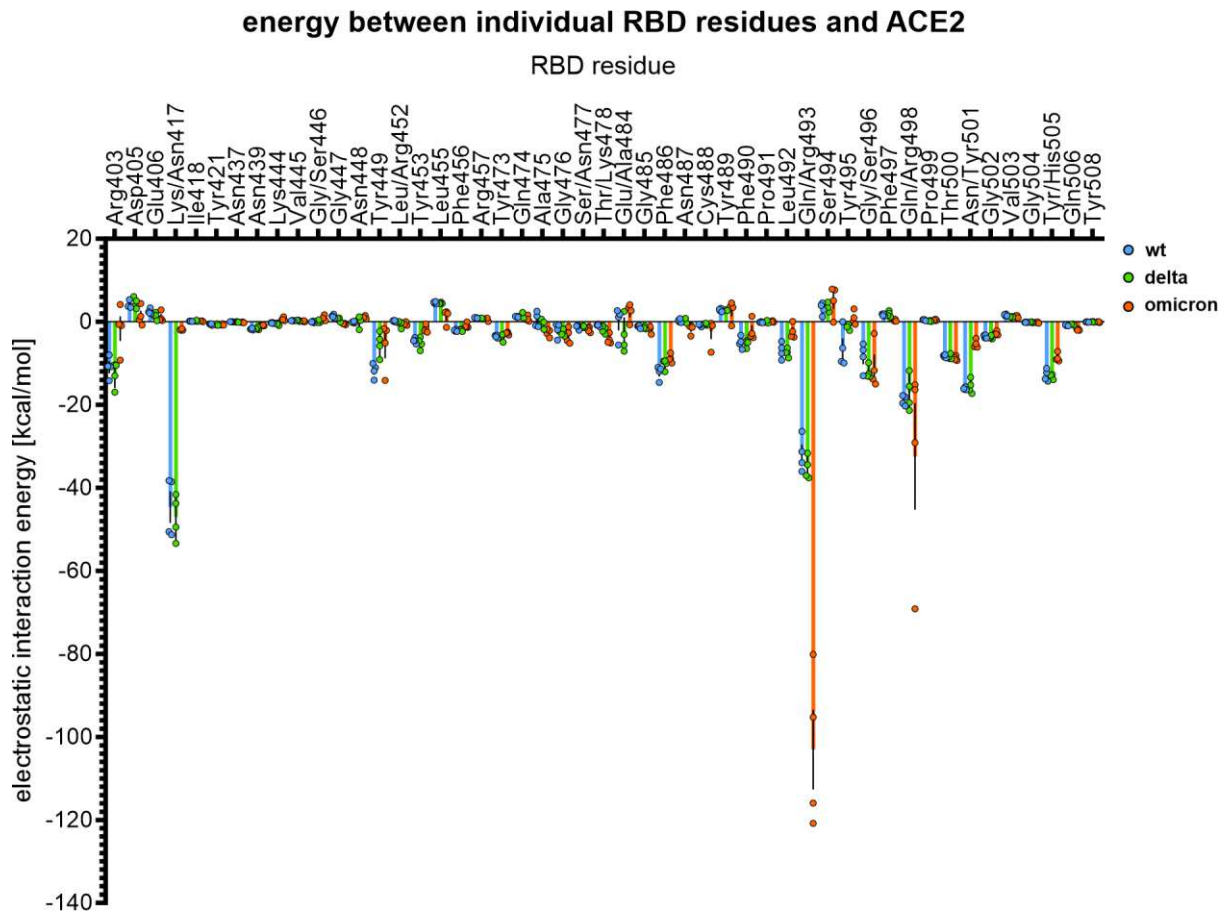
449 **Figure S2:**



450

451 **Figure S2:** **a**, Number of contacts for all residues of the RBD within 8 Å distance to ACE2 for wt, delta and omicron
452 variants. **b**, Number of contacts for residue 505 (tyrosine for wt and delta, histidine for omicron) formed with
453 ACE2. **c**, Structural representation of tyrosine 501 (Tyr501) and histidine 505 (His505) expressed on the RBD or
454 omicron and lysine 353 expressed on ACE2. **d**, Structural representation of number of contacts formed by the
455 epsilon (B.1.427/B.1.429) variant and the kappa (B.1.617.1) variant. Residues are shown in different color and
456 sphere size.

457 **Figure S3:**

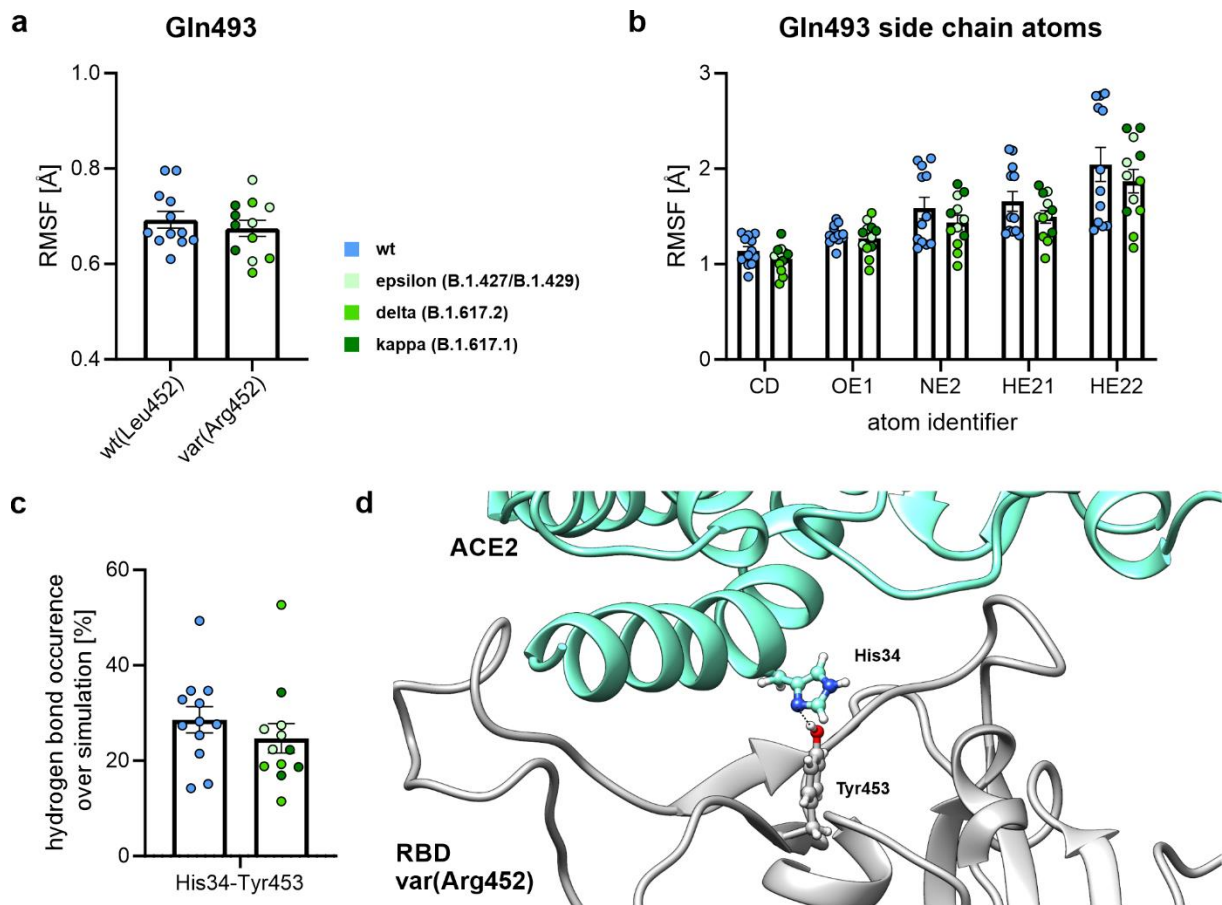


458

459 **Figure S3:** Linear electrostatic interaction energy for individual RBD residues expressed on the RBD–ACE2 inter-
460 face (within 8 Å distance from ACE2).

461

462 **Figure S4:**



463

464 **Figure S4: a**, Pooled comparison of the RMSF (root mean square fluctuation) values for glutamine 493 comparing
465 wt and L452R expressing variants. **b**, Detailed RMSF analysis of the side chain atoms of glutamine 493 comparing
466 wt and L452R expressing variants (epsilon: light green, delta: medium green, kappa: dark green). **c**, Hydrogen
467 bond occurrence between tyrosine 453 (Tyr453, RBD) and histidine 34 (His34, ACE2). **d**, Structural representation
468 of the hydrogen bond formed between tyrosine 453 (Tyr453, RBD with L452R) and histidine 34 (His34, ACE2).

469

470

471

472

473

474

475

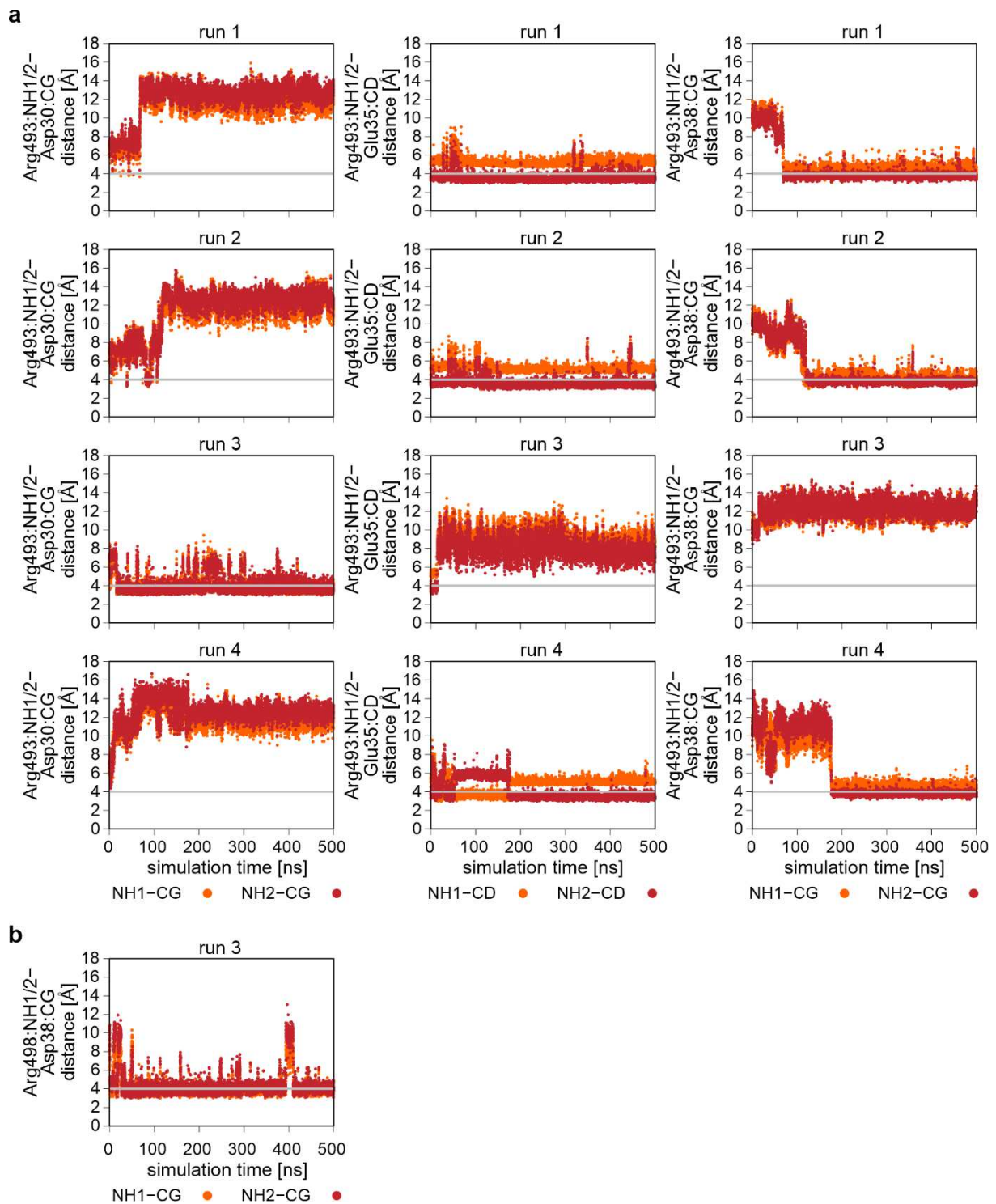
476

477

478

479

480



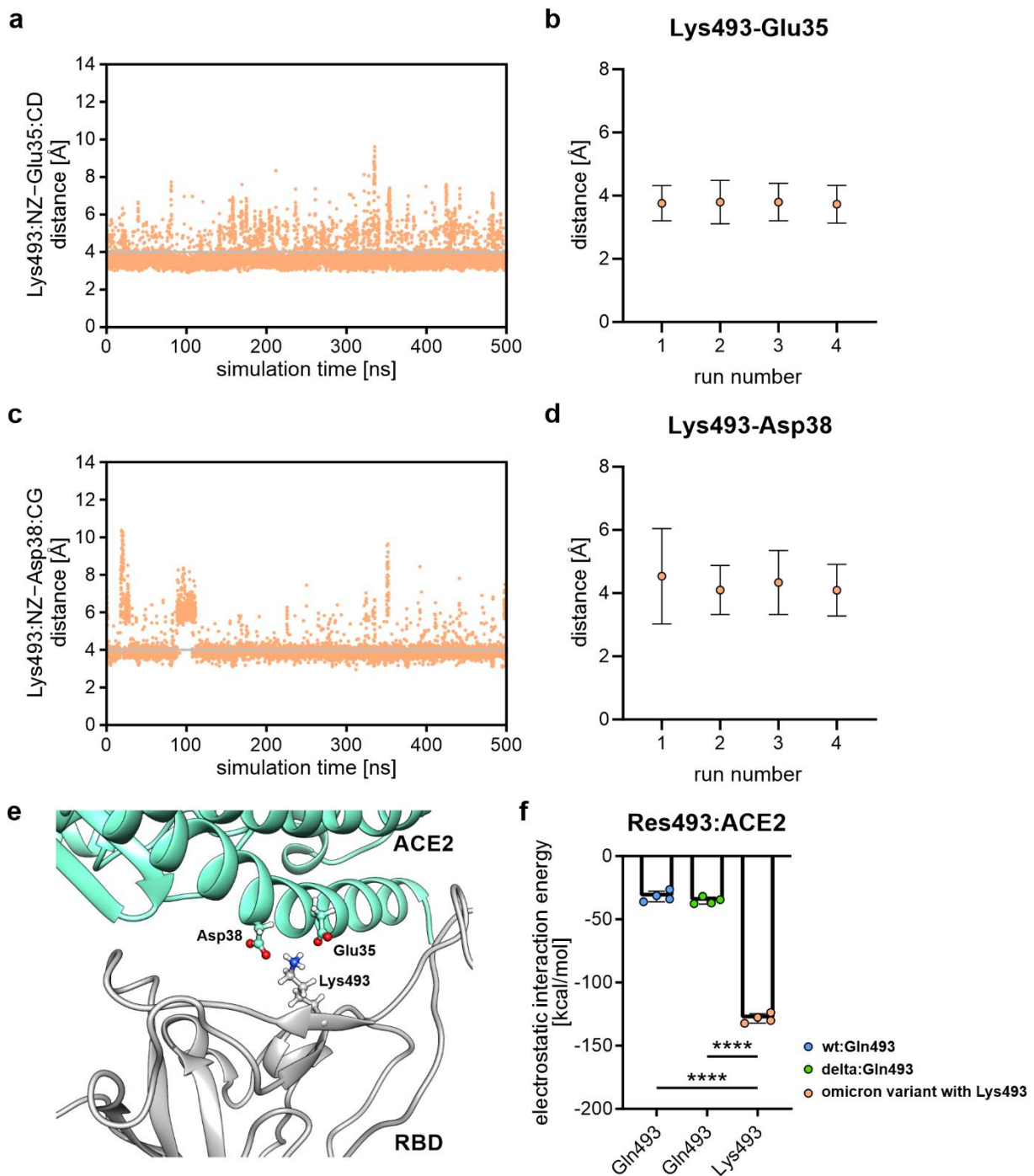
482

483 **Figure S5:** **a**, Time resolved distance plots of for individual MD simulation runs with distances plotted between
 484 arginine 493 (Arg493) expressed on the RBD and aspartate 30 (Asp30), glutamate 35 (Glu35) and aspartate 38
 485 (Asp38, all expressed on ACE2). **b**, time resolved distance plot from run 3 (a) for arginine 498 (Arg498) expressed
 486 on the RBD and aspartate 38 (Asp38) expressed on ACE2.

487

488

489



491

492 **Figure S6: a**, Representative distance plot of lysine 493 (RBD, omicron) and glutamate 35 (ACE2). **b**, Average
 493 distance with standard deviation error bars shown for four individual 500 ns runs for residues lysine 493 (RBD,
 494 omicron) and glutamate 35 (ACE2). **c**, Representative distance plot for lysine 493 (RBD, omicron) and aspartate
 495 38 (ACE2). **d**, Average distance with standard deviation error bars shown for four individual 500 ns runs for resi-
 496 dues lysine 493 (RBD, omicron) and aspartate 38 (ACE2). **e**, Structural representation of the two newly formed
 497 salt bridges between lysine 493 (Lys493) on the RBD and glutamate 35 (Glu35) and aspartate 38 (Asp38) both
 498 expressed on ACE2. **f**, Linear interaction energy for residue 493 analyzed for wt (blue), delta (green) and omicron
 499 (orange; **** $p < 0.0001$, one-way ANOVA).

500